

Bending rigidity and sound propagation in graphene

Unai Aseginolaza,^{1, 2, 3, *} Tommaso Cea,^{4, 5, 6} Raffaello Bianco,¹ Lorenzo Monacelli,⁵ Matteo Calandra,^{7, 8, 6} Aitor Bergara,^{1, 2, 9} Francesco Mauri,^{5, 6} and Ion Errea^{1, 2, 3, †}

¹*Centro de Física de Materiales CFM, CSIC-UPV/EHU,
Paseo Manuel de Lardizabal 5, 20018 Donostia, Basque Country, Spain*

²*Donostia International Physics Center (DIPC),
Manuel Lardizabal pasealekua 4, 20018 Donostia, Basque Country, Spain*

³*Fisika Aplikatua 1 Saila, University of the Basque Country (UPV/EHU),
Europa Plaza 1, 20018 Donostia, Basque Country, Spain*

⁴*Imdea Nanoscience, Faraday 9, 28015 Madrid, Spain*

⁵*Dipartimento di Fisica, Università di Roma La Sapienza, Piazzale Aldo Moro 5, I-00185 Roma, Italy*

⁶*Graphene Labs, Fondazione Instituto Italiano di Tecnologia, Italy*

⁷*Dipartimento di Fisica, Università di Trento, Via Sommarive 14, 38123 Povo, Italy.*

⁸*Sorbonne Universités, CNRS, Institut des Nanosciences de Paris, UMR7588, F-75252, Paris, France*

⁹*Departamento de Física de la Materia Condensada,*

University of the Basque Country (UPV/EHU), 48080 Bilbao, Basque Country, Spain

(Dated: December 22, 2024)

Despite the interest raised by graphene and 2D materials, their mechanical and acoustic properties are still highly debated. Harmonic theory predicts a quadratic dispersion for the flexural acoustic mode. Such a quadratic dispersion leads to diverging atomic fluctuations and a constant linewidth of in-plane acoustic phonon modes at small momentum, which implies that graphene cannot propagate sound waves. Many works based on membrane theory questioned the robustness of the quadratic dispersion, arguing that the anharmonic phonon-phonon interaction linearizes it, which implies a divergent bending rigidity (stiffness) in the long wavelength limit. However, these works are based on effective low-energy models that explicitly break the rotational invariance. Here we show that rotational symmetry protects the quadratic flexural dispersion against phonon-phonon interaction, and that the bending stiffness of graphene is unaffected by temperature and quantum fluctuations. Nevertheless, our non-perturbative anharmonic calculations predict that sound propagation coexists with such a quadratic dispersion. Since our conclusions are universal properties of membranes, they apply not just to graphene, but to all 2D materials.

Many of the applications of graphene are based on its uneven stiffness and high thermal conductivity^{1–3}. However, the mechanical, thermal, and acoustic properties of graphene, and in general of any 2D material, are far from being understood yet. Even the possibility of having crystalline order in 2D has been long questioned due to the diverging atomic displacements as a function of the sample size calculated in classical references^{4,5}. Experimentally, crystalline order has been observed in suspended graphene⁶, although it shows ripples that seem to be intrinsic according to many theoretical studies^{7–23}.

Most of the problems are caused by the quadratic dispersion of the acoustic flexural out-of-plane (ZA) mode that is obtained in the standard harmonic approximation. Such a quadratic dispersion also implies the unphysical result that graphene and other 2D membranes do not propagate sound. The phonon linewidths of the in-plane acoustic longitudinal (LA) and transverse (TA) phonons calculated perturbatively from the harmonic result do not vanish in the long wavelength limit²⁴, precisely, because of the quadratic dispersion of the ZA modes²⁵. This yields the conclusion that phonons having sufficiently small momentum do not live long enough for vibrating one period and the quasiparticle picture is lost, together with the propagation of sound.

It has been argued^{26–34} that the anharmonic coupling between in-plane and out-of-plane phonon modes renor-

malizes the dispersion of the ZA phonon modes, providing it with a linear term at small momenta that somewhat cures the pathologies. It has long been assumed^{7,35} as well that the out-of-plane vibrational frequency of any continuous membrane acquires a linear term at small wavevectors once interactions are included. Also that their bending rigidity diverges logarithmically in this limit, yielding the dubious interpretation that the larger the membrane, the stiffer it becomes. The experimental confirmation of these ideas is challenging due to the difficulties in measuring the bending rigidity of graphene^{36,37} and the substrate effects on the dispersion of the ZA modes measured with helium diffraction^{38–40}.

In this letter, by performing non-perturbative anharmonic calculations on graphene using both atomistic calculations and a membrane model, we convincingly show that a quadratic dispersion of the ZA mode in unstrained graphene, and any other 2D membrane, is actually expected and that it is compatible with well-defined sound waves. We also show that the bending stiffness of graphene is barely unaffected by phonon-phonon interactions. Our results are in stark contrast to the previously assumed behavior of membranes because we fully preserve rotational invariance and do not work with a low-energy model that breaks this symmetry.

In the harmonic approximation phonon frequencies are obtained diagonalizing the $\phi_{ab}/\sqrt{M_a M_b}$ dynamical ma-

trix, where a and b represent both atom and Cartesian indices, M_a is the mass of atom a , and $\phi_{ab} = \left[\frac{\partial V}{\partial R_a \partial R_b} \right]_0$ are the second-order force constants obtained as the second-order derivatives of the Born-Oppenheimer potential V with respect to atomic positions \mathbf{R} . Rotational symmetry, together with the fact that in a strictly two-dimensional system force constants involving an in-plane and an out-of-plane displacement vanish, makes the ZA mode acquire a quadratic dispersion close to zone center²⁸. Phonons expected experimentally, however, should be calculated from the imaginary part of the phonon Green's function that includes anharmonic effects⁴¹. For low energy modes, such as the ZA mode, dynamical effects can be safely neglected. In this limit the phonon peaks coincide with the eigenvalues of the free energy Hessian $\left[\frac{\partial F}{\partial R_a \partial R_b} \right]_0 / \sqrt{M_a M_b}$, where F is the anharmonic free energy and \mathbf{R} the average ionic positions⁴¹. This raises a formidable remark that has remained unnoticed thus far: as F and V obey the same symmetry properties, a $\sim q^2$ dispersion should be expected for the ZA mode both in the harmonic and anharmonic cases.

To account for anharmonicity beyond perturbation theory, we apply the self-consistent harmonic approximation (SCHA) in its stochastic implementation (SSCHA)⁴¹⁻⁴³ making use of a machine learning atomistic potential trained with density functional theory⁴⁴. We also solve the SCHA equations in a membrane continuum Hamiltonian. The SCHA is a variational method that minimizes the free energy of the system

$$F = \langle T + V + \frac{1}{\beta} \ln \rho_{\mathbf{R}\Phi} \rangle_{\rho_{\mathbf{R}\Phi}} \quad (1)$$

with respect to a density matrix $\rho_{\mathbf{R}\Phi}$ parametrized with centroid positions \mathbf{R} and effective force constants Φ (bold symbols represent vectors or tensors in compact notation). In Eq. (1) T is the ionic kinetic energy, β the inverse temperature, and $\langle O \rangle_{\rho_{\mathbf{R}\Phi}} = \text{tr}[\rho_{\mathbf{R}\Phi} O]$ (O is any operator). We call *auxiliary* the phonon frequencies obtained diagonalizing the $\Phi_{ab} / \sqrt{M_a M_b}$ matrix. These frequencies include non-perturbative anharmonic corrections as they result from the variational minimization of F that fully includes V . However, phonons probed experimentally are related to the peaks in the imaginary part of the interacting Green's function $G_{ab}(z)$ ⁴¹, which can be calculated from the

$$G_{ab}^{-1}(z) = G_{ab}^{-1(S)}(z) - \Pi_{ab}(z) \quad (2)$$

Dyson's equation. In Eq. (2) $G_{ab}^{-1(S)}(z) = z^2 \delta_{ab} - \Phi_{ab} / \sqrt{M_a M_b}$ is the non-interacting Green's function formed by the auxiliary phonons and $\Pi(z)$ is the phonon-phonon self-energy within the SCHA (see Supplementary Material⁴⁵). The peaks in the imaginary part of $G_{ab}(z)$ determine the frequencies and linewidths of the *physical* phonons. In the static $z = 0$ limit the peaks coincide with the eigenvalues of the free energy Hessian.

In order to calculate phonon spectra in unstrained graphene at any temperature, we calculate the SCHA

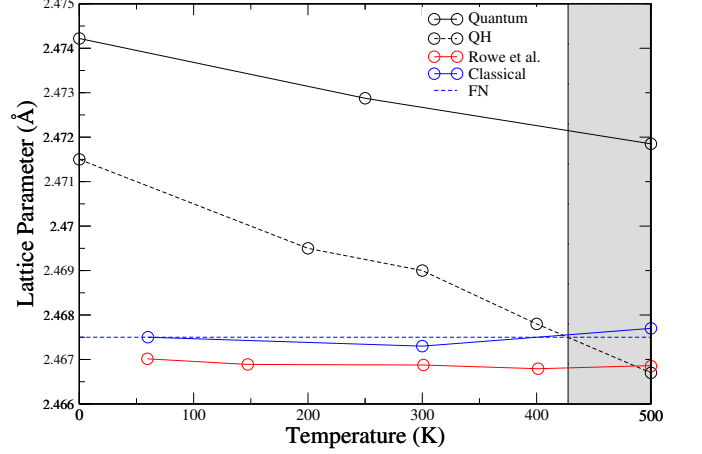


Figure 1. Lattice parameter of graphene as a function of temperature obtained with the SSCHA using a machine learning atomistic potential. Both quantum (black) and classical (blue) calculations are included. The classical result is calculated setting $\hbar = 0$ in the SCHA free energy. The temperature-independent frozen nuclei (FN) result corresponds to the lattice parameter that minimizes the Born Oppenheimer potential V . Results obtained by Rowe et al.⁴⁴ are included. The black dashed line corresponds to the quasi-harmonic result. In the grey zone harmonic phonons become unstable breaking down the quasiharmonic approximation.

stress tensor following the procedure in Ref. 43 and pick the lattice parameter that sets it to zero at each temperature. The lattice parameter calculated in this way includes anharmonic effects as well as the effect of quantum and thermal fluctuations. All the phonon spectra shown in this work obtained with the atomistic potential are calculated with the lattice parameter that gives a null stress at each temperature. The harmonic spectra on the contrary are always calculated at the lattice parameter that minimizes V . The temperature dependence of the lattice parameter is shown in Fig. 1. We include the molecular dynamics (MD) results of Rowe et al. obtained with the same potential⁴⁴, which do not account for quantum effects. For comparison, we also include SSCHA calculations in the classical limit, by making $\hbar = 0$ in $\rho_{\mathbf{R}\Phi}$, and within the quasiharmonic (QH) approximation. We expand our calculations up to 500 K, as below this temperature corrugations seem negligible^{29,49}. The centroid positions in the SCHA calculations are always in the plane. Our quantum calculations correctly capture the negative thermal expansion of graphene that has been estimated in previous theoretical works^{29,44}. Our SCHA result shows a larger lattice parameter than the classical result. This is not surprising as classical calculations neglect quantum fluctuations and, consequently, underestimate the fluctuations associated to the high-energy optical modes (the highest energy phonon modes require temperatures of around 2000 K to be thermally populated). This remarks the importance of considering quantum effects in the evaluation of thermodynamic properties of

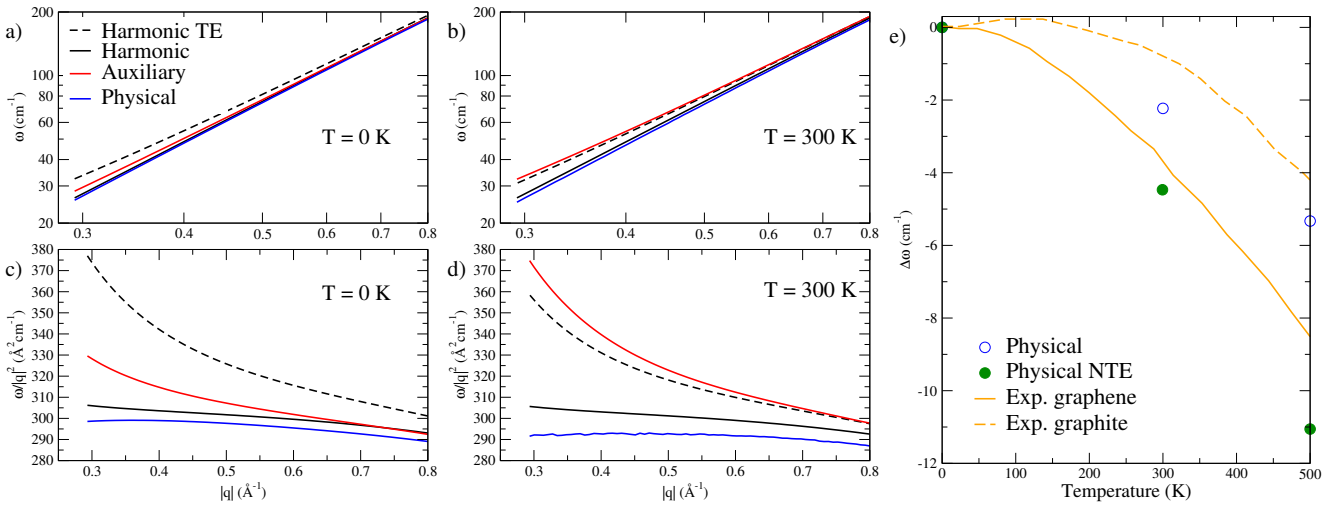


Figure 2. Harmonic ZA phonon spectra together with the SCHA auxiliary phonons and the physical phonons ascribed to the peaks of the Green's function in Eq. (2). Results at 0 K (a) and 300 K (b) are shown. (c) and (d) show the bending rigidity, defined as the frequency divided by the squared momentum. In the panels the dispersion corresponds to the Γ M direction. For reference, the M point is at 1.4662 \AA^{-1} at 0 K and at 1.4671 \AA^{-1} at 300 K. The harmonic result (solid black) is computed at the lattice parameter that minimizes V , while the other results include thermal expansion (see Fig. 1). The dashed black lines correspond to harmonic calculations including thermal expansion (TE). In (e) we show the temperature dependence of the frequency shift of the physical optical E_{2g} mode both considering thermal expansion and without considering it (NTE). We include experimental results in graphene⁴⁶ and graphite^{47,48}. All these calculations are performed with the machine learning atomistic potential.

graphene. Our classical results and the MD calculations of Rowe et al.⁴⁴ are in agreement (within their error of 0.0005 \AA). It is worth noting that the quasiharmonic approximation is not valid to calculate the thermal expansion of graphene due to the harmonic imaginary phonon frequencies that appear close to Γ for the ZA mode already at 500 K. In the shadowed region the QH is in principle not valid, even if it has been used with coarse integration grids that avoid the instabilities⁵⁰.

In Figs. 2 (a)-(d) we compare the harmonic phonon spectra with the auxiliary phonons as well as with the spectra obtained from the peaks in the imaginary part of the interacting Green's function, the physical phonons. The main conclusion is that while the dispersion of the ZA modes obtained from Φ is linearized, the physical phonons become close to a quadratic dispersion and approach the harmonic dispersion, as expected by symmetry in the static limit. This is very clear in Fig. 2(c) and (d), where we show that the bending rigidity, defined as the frequency divided by the squared momentum, is independent of the wavevector at any temperature. This suggests that the bending rigidity is barely affected by interactions, in contradiction to the broadly assumed result that it diverges logarithmically at small momentum in membranes due to thermal fluctuations⁷. In Fig. 2 (e) we show the temperature dependence of the frequency of the optical E_{2g} mode visible in Raman experiments, which red-shifts with increasing temperature in agreement with experiments^{47,48,51} and previous theoretical works⁵². The experimental results in graphene⁴⁶ lay between the shift calculated considering thermal expansion

and without considering it, which is the expected behavior due to the presence of the substrate.

Even if the anharmonic correction to the phonon spectra may look small in Fig. 2, it has a huge impact on the mechanical and thermal properties of graphene. When calculating the root mean square atomic displacement with the SCHA density matrix as $\sqrt{\langle \mathbf{u}^2 \rangle}_{\rho_{\mathcal{R}\Phi}}$, the dramatic divergences with the sample size obtained in the harmonic case are partially suppressed (see Supplementary Material⁴⁵), clearly showing the contribution of anharmonicity to the mechanical stability of graphene. The divergences reduce precisely because the auxiliary phonons that build $\rho_{\mathcal{R}\Phi}$ are linear at small momenta (see Fig. 2). Thus, even if the phonons obtained from the SCHA Green's function are quadratic, the fact that the density matrix used to compute thermodynamic properties is built with linearized phonons makes the divergences reduce.

As shown in Fig. 3, the SCHA non-perturbative calculation based on Eq. (2) dramatically changes the linewidth of the LA and TA modes at small momenta by making them smaller as momentum decreases, in clear contrast to the perturbative calculation obtained on top of the harmonic result. This happens thanks to the linearization of the auxiliary acoustic phonons at small momentum. When the ratio between the full-width at half-maximum (FWHM) and the frequency of the mode is approximately 1, the quasiparticle picture is lost. This value is reached in the $0.001\text{--}0.002 \text{ \AA}^{-1}$ momentum range in the harmonic case. However, when the linewidth is calculated within the SCHA, the ratio never gets big-

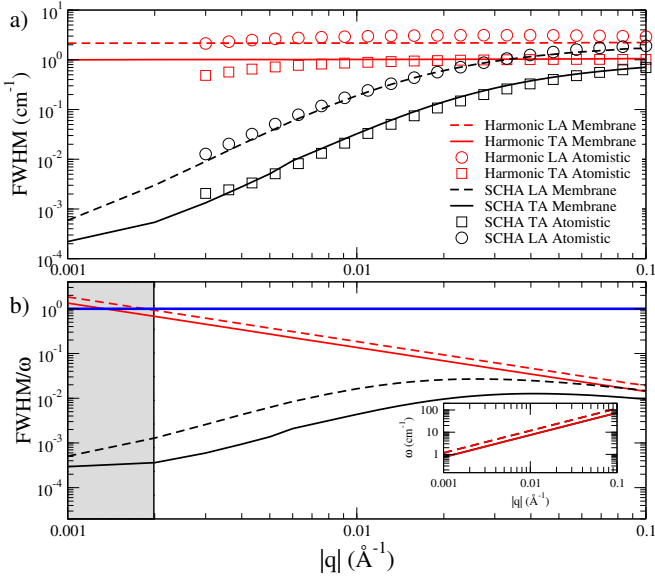


Figure 3. (a) Linewidths (full width at half maximum) of LA and TA phonon modes at 300 K calculated within perturbation theory on top of the harmonic result and within the SCHA following Eq. (2). Squares and circles are calculated with the atomistic potential. Lines correspond to calculations done with the membrane model in Eq. 3. Our harmonic results are in good agreement with other theoretical calculations^{24,25}. (b) FWHM divided by the phonon frequency in the membrane model. In the inset we show the phonon frequencies in the same momentum range. The grey zone corresponds to the region where the fraction $\text{FWHM}_{\text{LA}}/\omega_{\text{LA}}$ is bigger than one in the harmonic case.

ger than 0.05. These results recover the quasiparticle picture for these modes at any wavevector, guaranteeing that graphene always propagates sound. The momentum range for which the quasiparticle picture is lost in the harmonic approximation can be reached experimentally with Brillouin scattering probes. In fact, for few layer graphene the quasiparticle picture holds in the 0.001–0.002 Å⁻¹ region⁵³, in agreement with our calculations. We show here that there is no need of strain²⁵ to have physically well-defined phonon linewidths in graphene.

In order to obtain results at very small momenta and reinforce the conclusions drawn with the atomistic calculations, we solve the SCHA equations in a continuum membrane Hamiltonian. This model has been widely used in the literature to describe graphene as an elastic membrane as well as to account for the coupling between in-plane and out-of plane acoustic modes^{7,30–32,35}. The most general rotationally invariant continuum potential to describe a free-standing 2D membrane up to the fourth-order in the phonon fields has the following form⁵⁴:

$$V = \frac{1}{2} \int_{\Omega} d^2x (\kappa(\partial^2 h)^2 + C^{ijkl} u_{ij} u_{kl}), \quad (3)$$

$$u_{ij} = \frac{1}{2} (\partial_i u_j + \partial_j u_i + \partial_i \mathbf{u} \cdot \partial_j \mathbf{u} + \partial_i h \partial_j h). \quad (4)$$

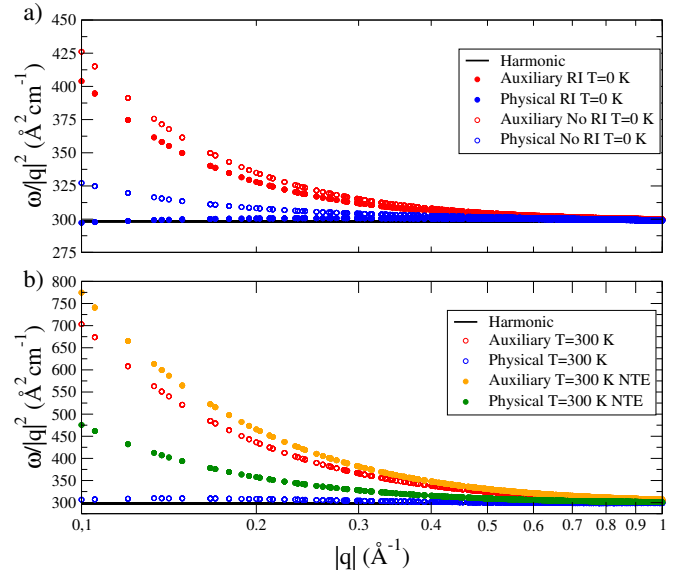


Figure 4. (a) Bending rigidity of graphene, defined as the ratio between the frequency of the ZA mode divided by the squared momentum, calculated within the harmonic approximation and within the SCHA auxiliary and physical cases at 0 K in the membrane model. We name rotationally invariant (RI) the results considering the full potential in Eq. 3. We name no rotationally invariant (No RI) the results neglecting the $\partial_i \mathbf{u} \cdot \partial_j \mathbf{u}$ term in Eq. (4). (b) Same results at 300 K with the full membrane potential. We also include the results without considering thermal expansion (NTE).

Here $\mathbf{u}(\mathbf{x})$ and $h(\mathbf{x})$ are the in-plane and out-of-plane displacement fields, respectively, u_{ij} is the stress tensor, and \mathbf{x} is the 2D position vector in the membrane. κ is the harmonic bending rigidity of the membrane, Ω is the area of the membrane, and the tensor $C^{ijkl} = \lambda \delta^{ij} \delta^{kl} + \mu (\delta^{ik} \delta^{jl} + \delta^{il} \delta^{jk})$ contains the Lamé coefficients λ and μ and Kronecker deltas. We have calculated the parameters by fitting them to the atomistic potential, which yields $\lambda = 4.3 \text{ eV} \text{\AA}^{-2}$, $\mu = 9.3 \text{ eV} \text{\AA}^{-2}$, $\kappa = 1.5 \text{ eV}$ and, $\rho/\hbar^2 = 1097 \text{ eV} \text{\AA}^{-4}$. This continuum model only accounts for acoustic modes. The harmonic acoustic frequencies given by Eq. (3) are $\omega_{ZA}(q) = \sqrt{\kappa/\rho q^2}$, $\omega_{LA}(q) = \sqrt{(\lambda + \mu)/\rho q}$, and $\omega_{TA}(q) = \sqrt{\mu \rho q}$, ρ being the mass density of the membrane. The thermal expansion is included in this formalism by changing the in-plane derivatives as $\partial_i u_j \rightarrow \partial_i u_j + \delta^{ij} \delta a$, with $\delta a = (a - a_0)/a_0$, a_0 being the lattice parameter that minimizes V .

The results obtained in this rotationally invariant membrane are shown in Fig. 4. All conclusions drawn with the atomistic model are confirmed and put in solid grounds. Again the ZA phonons obtained from the auxiliary SCHA force constants get linearized at small momenta. However, when the physical phonons are calculated from the Hessian of the SCHA free energy (due to the low frequencies of the ZA modes this static approximation is perfectly valid as shown in the Supplementary Material⁴⁵), the ZA phonon frequencies get basically on

top of the harmonic values recovering a quadratic dispersion. This means that the physical phonons have a quadratic dispersion for small momenta in an unstrained membrane, as it is expected by symmetry, and that the bending rigidity does not increase in the long wavelength limit and is barely affected by interactions. Our results thus upturn the conventional wisdom of 2D membranes^{7,30–32,35}: interactions do not linearize the dispersion of the ZA mode and the bending rigidity does not diverge at small momentum. The main reason for this is that in previous works the $\partial_i \mathbf{u} \cdot \partial_j \mathbf{u}$ term in the stress tensor, which guarantees rotational invariance, is neglected, unavoidably lowering the power of the ZA phonon frequency to $\sim q^d$, with $1 \leq d < 2$, as shown in Fig. 4(a). We also show that accounting correctly for the thermal expansion is crucial to recover the quadratic dispersion of the flexural modes. Finally, we calculate the linewidths of the LA and TA modes in the membrane model in the perturbative case on top of the harmonic result and within the SCHA (see, Fig. 3). Again, the results show how the quasiparticle picture is lost in the harmonic case, while it is completely recovered in the SCHA. The linewidths calculated in the atomistic case and within the membrane model are surprisingly close. This means that the simple empirical coefficients that parametrize the membrane po-

tential capture all the anharmonicity that affects acoustic modes in graphene.

In conclusion, we show that anharmonic effects are crucial to make sound propagate in graphene. Moreover, we determine that, despite the relevance of anharmonic effects, the out-of-plane acoustic modes should show a quadratic dispersion experimentally. We estimate anharmonic effects within the self-consistent harmonic approximation both with an atomistic machine learning potential and with a membrane model, obtaining consistent results in both cases. These conclusions can be extrapolated to any strictly 2D material or membrane, and will have a large impact on the understanding of their mechanical, vibrational, and thermal properties.

We would like to thank Francisco Guinea for useful conversations. Financial support was provided by the Spanish Ministry of Economy and Competitiveness (FIS2016-76617-P); the Department of Education, Universities and Research of the Basque Government and the University of the Basque Country (IT756-13); and the European Commission under the Graphene Flagship, Core 3, grant number 881603. U.A. is also thankful to the Material Physics Center for a predoctoral fellowship. Computer facilities were provided by the Donostia International Physics Center (DIPC).

* uaseguinolaz001@ehu.eus
† ion.errea@ehu.eus

- ¹ W. Kong, H. Kum, S.-H. Bae, J. Shim, H. Kim, L. Kong, Y. Meng, K. Wang, C. Kim, and J. Kim, *Nature Nanotechnology* **14**, 927 (2019).
- ² C. Lee, X. Wei, J. W. Kysar, and J. Hone, *science* **321**, 385 (2008).
- ³ d. Ghosh, I. Calizo, D. Teweldebrhan, E. P. Pokatilov, D. L. Nika, A. A. Balandin, W. Bao, F. Miao, and C. N. Lau, *Applied Physics Letters* **92**, 151911 (2008).
- ⁴ L. D. Landau and E. M. Lifshitz, *Statistical Physics* (Pergamon, 1980).
- ⁵ N. D. Mermin, *Physical Review* **176**, 250 (1968).
- ⁶ J. C. Meyer, A. K. Geim, M. I. Katsnelson, K. S. Novoselov, T. J. Booth, and S. Roth, *Nature* **446**, 60 (2007).
- ⁷ Nelson, D.R. and Peliti, L., *J. Phys. France* **48**, 1085 (1987).
- ⁸ A. Fasolino, J. H. Los, and M. I. Katsnelson, *Nature Materials* **6**, 858 (2007).
- ⁹ D. Gazit, *Phys. Rev. B* **80**, 161406 (2009).
- ¹⁰ D. Gazit, *Phys. Rev. E* **80**, 041117 (2009).
- ¹¹ P. San-Jose, J. González, and F. Guinea, *Phys. Rev. Lett.* **106**, 045502 (2011).
- ¹² L. L. Bonilla and A. Carpio, *Journal of Statistical Mechanics: Theory and Experiment* **2012**, P09015 (2012).
- ¹³ F. Guinea, P. Le Doussal, and K. J. Wiese, *Phys. Rev. B* **89**, 125428 (2014).
- ¹⁴ J. González, *Phys. Rev. B* **90**, 165402 (2014).
- ¹⁵ M. Ruiz-Garcia, L. Bonilla, and A. Prados, *Journal of Statistical Mechanics: Theory and Experiment* **2015** (2015), 10.1088/1742-5468/2015/05/P05015.
- ¹⁶ I. V. Gornyi, V. Y. Kachorovskii, and A. D. Mirlin, *Phys. Rev. B* **92**, 155428 (2015).
- ¹⁷ M. Ruiz-García, L. L. Bonilla, and A. Prados, *Phys. Rev. B* **94**, 205404 (2016).
- ¹⁸ L. L. Bonilla and M. Ruiz-Garcia, *Phys. Rev. B* **93**, 115407 (2016).
- ¹⁹ I. V. Gornyi, A. P. Dmitriev, A. D. Mirlin, and I. V. Protopopov, *Journal of Experimental and Theoretical Physics* **123**, 322 (2016).
- ²⁰ M. Ruiz-Garcia, L. L. Bonilla, and A. Prados, *Phys. Rev. E* **96**, 062147 (2017).
- ²¹ T. Cea, M. Ruiz-Garcia, L. Bonilla, and F. Guinea, arXiv e-prints , arXiv:1911.10536 (2019), arXiv:1911.10536 [cond-mat.soft].
- ²² T. Cea, M. Ruiz-Garcia, L. Bonilla, and F. Guinea, arXiv e-prints , arXiv:1911.10510 (2019), arXiv:1911.10510 [cond-mat.mes-hall].
- ²³ J. A. Silva-Guillén and F. Guinea, *Phys. Rev. B* **101**, 060102 (2020).
- ²⁴ L. Paulatto, F. Mauri, and M. Lazzeri, *Physical Review B* **87**, 214303 (2013).
- ²⁵ N. Bonini, J. Garg, and N. Marzari, *Nano letters* **12**, 2673 (2012).
- ²⁶ H. Wang and M. S. Daw, *Physical Review B* **94**, 155434 (2016).
- ²⁷ J. Los, M. I. Katsnelson, O. Yazyev, K. Zakharchenko, and A. Fasolino, *Physical Review B* **80**, 121405 (2009).
- ²⁸ M. I. Katsnelson and A. Fasolino, *Accounts of chemical research* **46**, 97 (2013).
- ²⁹ K. Zakharchenko, M. Katsnelson, and A. Fasolino, *Physical review letters* **102**, 046808 (2009).
- ³⁰ E. Mariani and F. Von Oppen, *Physical review letters* **100**,

076801 (2008).

³¹ B. Amorim, R. Roldán, E. Cappelluti, A. Fasolino, F. Guinea, and M. Katsnelson, *Physical Review B* **89**, 224307 (2014).

³² P. De Andres, F. Guinea, and M. Katsnelson, *Physical Review B* **86**, 144103 (2012).

³³ K. H. Michel, S. Costamagna, and F. M. Peeters, *Phys. Rev. B* **91**, 134302 (2015).

³⁴ K. H. Michel, P. Scuracchio, and F. M. Peeters, *Phys. Rev. B* **96**, 094302 (2017).

³⁵ P. Le Doussal and L. Radzihovsky, *Phys. Rev. Lett.* **69**, 1209 (1992).

³⁶ M. K. Blees, A. W. Barnard, P. A. Rose, S. P. Roberts, K. L. McGill, P. Y. Huang, A. R. Ruyack, J. W. Kevek, B. Kobrin, D. A. Muller, and P. L. McEuen, *Nature* **524**, 204 (2015).

³⁷ N. Lindahl, D. Midtvedt, J. Svensson, O. A. Nerushev, N. Lindvall, A. Isacsson, and E. E. B. Campbell, *Nano Letters* **12**, 3526 (2012).

³⁸ A. al Taleb, G. Anemone, D. Farías, and R. Miranda, *Carbon* **99**, 416 (2016).

³⁹ A. Al Taleb, H. K. Yu, G. Anemone, D. Farías, and A. M. Wodtke, *Carbon* **95**, 731 (2015).

⁴⁰ A. Al Taleb, G. Anemone, D. Farías, and R. Miranda, *Carbon* **133**, 31 (2018).

⁴¹ R. Bianco, I. Errea, L. Paulatto, M. Calandra, and F. Mauri, *Physical Review B* **96**, 014111 (2017).

⁴² I. Errea, M. Calandra, and F. Mauri, *Physical Review B* **89**, 064302 (2014).

⁴³ L. Monacelli, I. Errea, M. Calandra, and F. Mauri, *Physical Review B* **98**, 024106 (2018).

⁴⁴ P. Rowe, G. Csányi, D. Alfè, and A. Michaelides, *Physical Review B* **97**, 054303 (2018).

⁴⁵ See Supplementary Material for further details on the calculation, i.e., the dynamic SCHA theory, the machine learning potential, and the membrane model. The Supplementary Material cites all these references 41–44, 55–60.

⁴⁶ S. Linas, Y. Magnin, B. Poinsot, O. Boisron, G. Förster, V. Martinez, R. Fulcrand, F. Tournus, V. Dupuis, F. Rabilloud, *et al.*, *Physical Review B* **91**, 075426 (2015).

⁴⁷ H. Kagi, I. Tsuchida, M. Wakatsuki, K. Takahashi, N. Kamimura, K. Iuchi, and H. Wada, *Geochimica et Cosmochimica Acta* **58**, 3527 (1994).

⁴⁸ P. Tan, Y. Deng, Q. Zhao, and W. Cheng, *Applied physics letters* **74**, 1818 (1999).

⁴⁹ M. Pozzo, D. Alfe, P. Lacovig, P. Hofmann, S. Lizzit, and A. Baraldi, *Physical review letters* **106**, 135501 (2011).

⁵⁰ N. Mounet and N. Marzari, *Phys. Rev. B* **71**, 205214 (2005).

⁵¹ I. Calizo, A. Balandin, W. Bao, F. Miao, and C. Lau, *Nano letters* **7**, 2645 (2007).

⁵² N. Bonini, M. Lazzeri, N. Marzari, and F. Mauri, *Physical review letters* **99**, 176802 (2007).

⁵³ Z. Wang, H. Lim, S. Ng, B. Özyilmaz, and M. Kuok, *Carbon* **46**, 2133 (2008).

⁵⁴ L. D. Landau and E. M. Lifshit's, *Theory of elasticity*, by Landau, LD; Lifshit's, EM London, Pergamon Press; Reading, Mass., Addison-Wesley Pub. Co., 1959. Addison-Wesley physics books (1959).

⁵⁵ M. Dion, H. Rydberg, E. Schröder, D. C. Langreth, and B. I. Lundqvist, *Physical review letters* **92**, 246401 (2004).

⁵⁶ J. P. Perdew, K. Burke, and M. Ernzerhof, *Physical review letters* **77**, 3865 (1996).

⁵⁷ D. Vanderbilt, *Physical review B* **41**, 7892 (1990).

⁵⁸ V. Barone, M. Casarin, D. Forrer, M. Pavone, M. Sambi, and A. Vittadini, *Journal of computational chemistry* **30**, 934 (2009).

⁵⁹ H. J. Monkhorst and J. D. Pack, *Physical review B* **13**, 5188 (1976).

⁶⁰ T. J. Ypma, *SIAM review* **37**, 531 (1995).

Supplementary Material:

Bending rigidity and sound propagation in graphene

Unai Aseginolaza^{1,2,3}, Tommaso Cea^{4,5,6}, Raffaello Bianco¹, Lorenzo Monacelli⁵, Matteo Calandra^{7,8,6}, Francesco Mauri^{5,6}, Aitor Bergara^{1,2,9}, and Ion Errea^{1,2,3}

¹Centro de Física de Materiales CFM, CSIC-UPV/EHU, Paseo Manuel de Lardizabal 5, 20018 Donostia, Basque Country, Spain

²Donostia International Physics Center (DIPC), Manuel Lardizabal pasealekua 4, 20018 Donostia, Basque Country, Spain

³Fisika Aplikatua 1 Saila, University of the Basque Country (UPV/EHU), Europa Plaza 1, 20018 Donostia, Basque Country, Spain

⁴Imdea Nanoscience, Faraday 9, 28015 Madrid, Spain

⁵Dipartimento di Fisica, Università di Roma La Sapienza, Piazzale Aldo Moro 5, I-00185 Roma, Italy

⁶Graphene Labs, Fondazione Istituto Italiano di Tecnologia, Italy

⁷Dipartimento di Fisica, Università di Roma La Sapienza, Piazzale Aldo Moro 5, I-00185 Roma, Italy

⁸Sorbonne Universités, CNRS, Institut des Nanosciences de Paris, UMR7588, F-75252, Paris, France

⁹Departamento de Física de la Materia Condensada, University of the Basque Country (UPV/EHU), 48080 Bilbao, Basque Country, Spain

1 Anharmonic theory: SCHA

We study the lattice dynamics of graphene in the Born-Oppenheimer (BO) approximation, thus we consider the quantum Hamiltonian for the atoms defined by the BO potential energy $V(\mathbf{R})$. With \mathbf{R} we are denoting in component-free notation the quantity $R^{s\alpha}(\mathbf{l})$, which is a collective coordinate that completely specifies the atomic configuration of the crystal. The index α denotes the Cartesian direction, s labels the atom within the unit cell and \mathbf{l} indicates the three dimensional lattice vector. In what follows we will also use a single composite index $a = (\alpha, s, \mathbf{l})$ to indicate Cartesian index α , atom s index and lattice vector \mathbf{l} . Moreover, in general, we will use bold letters to indicate also other quantities in component-free notation.

In order to take into account quantum effects and anharmonicity at a non-perturbative level, we use the Self-Consistent Harmonic Approximation[1, 2, 3] (SCHA). For a given temperature T , the method allows to find an approximation for $F(\mathcal{R})$, the free energy of the crystal as a function of the average atomic positions \mathcal{R}^a (the centroids). For a given centroid \mathcal{R} , the SCHA free energy is obtained through an auxiliary quadratic Hamiltonian, the SCHA Hamiltonian $\mathcal{H}_{\mathcal{R}\Phi}$, by variationally minimizing the free energy with respect to the SCHA centroids and 2 body forces-constants (2BFC) Φ . The density matrix associated to the SCHA Hamiltonian is used in this work to calculate the expected values of physical observables, such as, the atomic displacements. The free energy Hessian, or the physical phonons in the static approach, can be computed by using the analytic formula (in component-free notation)

$$\frac{\partial^2 F}{\partial \mathcal{R} \partial \mathcal{R}} = \Phi + \overset{(3)}{\Phi} \Lambda(0) [1 - \overset{(4)}{\Phi} \Lambda(0)]^{-1} \overset{(3)}{\Phi}, \quad (1)$$

with

$$\Phi = \left\langle \frac{\partial^2 V}{\partial \mathbf{R} \partial \mathbf{R}} \right\rangle_{\rho_{\mathcal{R}\Phi}}, \overset{(3)}{\Phi} = \left\langle \frac{\partial^3 V}{\partial \mathbf{R} \partial \mathbf{R} \partial \mathbf{R}} \right\rangle_{\rho_{\mathcal{R}\Phi}}, \overset{(4)}{\Phi} = \left\langle \frac{\partial^4 V}{\partial \mathbf{R} \partial \mathbf{R} \partial \mathbf{R} \partial \mathbf{R}} \right\rangle_{\rho_{\mathcal{R}\Phi}}, \quad (2)$$

where the averages are with respect to the density matrix of the SCHA Hamiltonian $\mathcal{H}_{\mathcal{R}\Phi}$. i.e $\rho_{\mathcal{R}\Phi} = e^{-\beta \mathcal{H}_{\mathcal{R}\Phi}} / \text{tr}[e^{-\beta \mathcal{H}_{\mathcal{R}\Phi}}]$, and $\beta = (K_B T)^{-1}$ where K_B is the Boltzmann constant. In Eq. 1 the value $z = 0$ of the 4th-order tensor $\Lambda(z)$ is used. For a generic complex number z it is defined, in components, by

$$\Lambda^{abcd}(z) = -\frac{1}{2} \sum_{\mu\nu} \tilde{F}(z, \tilde{\Omega}_\mu, \tilde{\Omega}_\nu) \times \sqrt{\frac{\hbar}{2M_a \tilde{\Omega}_\mu}} e_\mu^a \sqrt{\frac{\hbar}{2M_b \tilde{\Omega}_\nu}} e_\nu^b \sqrt{\frac{\hbar}{2M_c \tilde{\Omega}_\mu}} e_\mu^c \sqrt{\frac{\hbar}{2M_d \tilde{\Omega}_\nu}} e_\nu^d, \quad (3)$$

with M_a the mass of the atom a , $\tilde{\Omega}_\mu^2$ (the *auxiliary* phonons) and e_μ^a eigenvalues and corresponding eigenvectors of $D_{ab}^{(S)} = \Phi_{ab} / \sqrt{M_a M_b}$, respectively, and

$$\tilde{F}(z, \tilde{\Omega}_\mu, \tilde{\Omega}_\nu) = \frac{2}{\hbar} \left[\frac{(\tilde{\Omega}_\mu + \tilde{\Omega}_\nu)[1 + n_B(\tilde{\Omega}_\mu) + n_B(\tilde{\Omega}_\nu)]}{(\tilde{\Omega}_\mu + \tilde{\Omega}_\nu)^2 - z^2} - \frac{(\tilde{\Omega}_\mu - \tilde{\Omega}_\nu)[n_B(\tilde{\Omega}_\mu) - n_B(\tilde{\Omega}_\nu)]}{(\tilde{\Omega}_\mu - \tilde{\Omega}_\nu)^2 - z^2} \right] \quad (4)$$

where $n_B(\omega) = 1/(e^{\beta \hbar \omega} - 1)$ is the bosonic occupation number.

As shown in ref. [2], in the context of the SCHA it is possible to formulate an ansatz in order to give an approximate expression to the one-phonon Green function $\mathbf{G}(z)$ for the variable $\sqrt{M_a}(R^a - \mathcal{R}^a)$:

$$\mathbf{G}^{-1}(z) = z^2 \mathbf{1} - \mathbf{M}^{-\frac{1}{2}} \Phi \mathbf{M}^{-\frac{1}{2}} - \mathbf{\Pi}(z), \quad (5)$$

where $\mathbf{G}^{-1}(0) = -\mathbf{D}^{(F)}$, $D_{ab}^{(F)} = \frac{1}{\sqrt{M_a M_b}} \frac{\partial^2 F}{\partial \mathcal{R}_a \partial \mathcal{R}_b}$, and $\mathbf{\Pi}(z)$ is the SCHA self-energy, given by

$$\mathbf{\Pi}(z) = \mathbf{M}^{-\frac{1}{2}} \overset{(3)}{\Phi} \Lambda(z) [1 - \overset{(4)}{\Phi} \Lambda(z)]^{-1} \overset{(3)}{\Phi} \mathbf{M}^{-\frac{1}{2}}, \quad (6)$$

where $M_{ab} = \delta_{ab} M_a$ is the mass matrix. For the applications considered in the present paper, the static term $\overset{(4)}{\Phi} \Lambda(0)$ is negligible with respect to the identity matrix (see Fig. 1). Extending

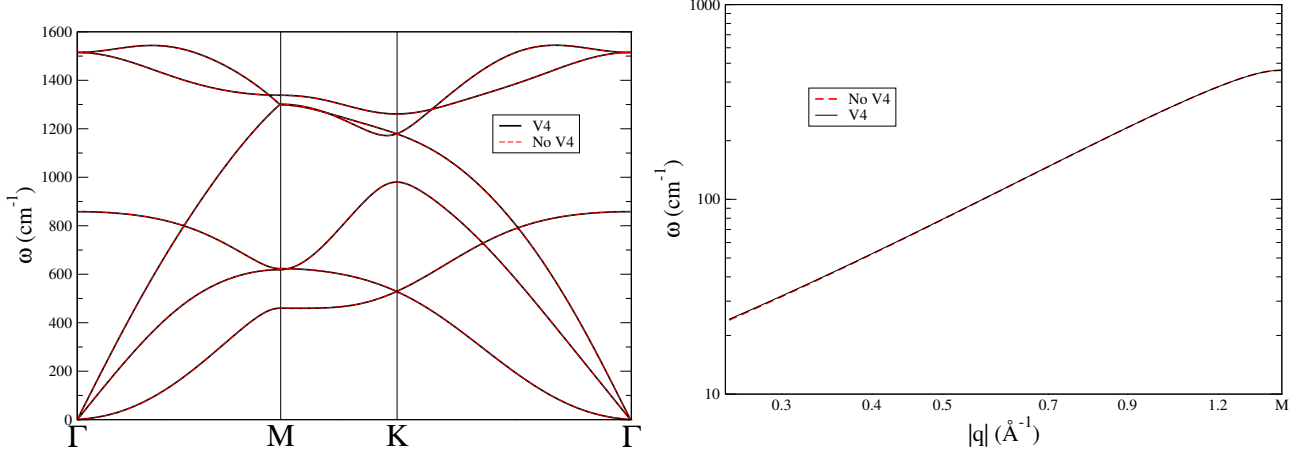


Figure 1: Physical phonons in the static approach at 500 K with and without including the 4BFC. The right panel only includes the ZA modes and it is in logarithmic scale. The calculation is done in a 6×6 supercell. $M = 1.4675 \text{ \AA}^{-1}$.

this approximation to the dynamical case reduces the SCHA self-energy to the so called bubble self-energy, namely

$$\Pi \approx \Pi^{(B)}(z) = \mathbf{M}^{-\frac{1}{2}} \mathbf{\Phi} \mathbf{\Lambda}(z) \mathbf{\Phi} \mathbf{M}^{-\frac{1}{2}}. \quad (7)$$

We then neglect the mixing between different phonon modes and assume that $\Pi(z)$ is diagonal in the basis of the eigenvectors $e_\mu^a(\mathbf{q})$ of $\Phi_{ab}(\mathbf{q})/\sqrt{M_a M_b}$ where $\Phi_{ab}(\mathbf{q})$ is the Fourier transform of the real space Φ (now a and b represent atoms in the unit cell and Cartesian indices). We then define

$$\Pi_\mu(\mathbf{q}, \omega) = \sum_{a,b} e_\mu^a(-\mathbf{q}) \Pi_{ab}(\mathbf{q}, \omega + i0^+) e_\mu^b(\mathbf{q}). \quad (8)$$

In studying the response of a lattice to inelastic scattering experiments we need the one-phonon spectral function. By using Eq. 5 for $\mathbf{G}(z)$ we can calculate the cross-section $\sigma(\omega) = -\omega \text{Tr} \text{Im} \mathbf{G}(\omega + i0^+)/\pi$, whose peaks signal the presence of collective vibrational excitations (physical phonons in the dynamic approach) having certain energies. Again, we take advantage of the lattice periodicity and we Fourier transform the interesting quantities with respect to the lattice indices. In particular, we consider the Fourier transform of the SCHA self-energy, $\Pi_{ab}(\mathbf{q}, z)$. Neglecting the mixing between different modes, the cross section is then given by

$$\sigma(\mathbf{q}, \omega) = \frac{1}{\pi} \sum_\mu \frac{-\omega \text{Im} \Pi_\mu(\mathbf{q}, \omega)}{(\omega^2 - \tilde{\Omega}_\mu^2(\mathbf{q}) - \text{Re} \Pi_\mu(\mathbf{q}, \omega))^2 + (\text{Im} \Pi_\mu(\mathbf{q}, \omega))^2}. \quad (9)$$

If we neglect the frequency dependence of the phonon self-energy, we get the weakly anharmonic limit of the cross section, which is going to be a sum of Lorentzian functions. These Lorentzians are well defined physical phonons in the dynamical approach. The phonon frequencies squared, $\Omega_\mu^2(\mathbf{q})$, corrected by the bubble self-energy are obtained as

$$\Omega_\mu^2(\mathbf{q}) = \tilde{\Omega}_\mu^2(\mathbf{q}) + \text{Re} \Pi_\mu(\mathbf{q}, \tilde{\Omega}_\mu(\mathbf{q})), \quad (10)$$

where $\tilde{\Omega}_\mu^2(\mathbf{q})$ are the eigenvalues of the Fourier transform of $\mathbf{D}^{(S)}$. The linewidth of the phonons in Eq. 10 is proportional to $Im\Pi_\mu(\mathbf{q}, \tilde{\Omega}_\mu(\mathbf{q}))$. The centers of these peaks are the ones supposed to be measured in inelastic experiments. By calculating $\tilde{\Omega}_\mu^2(\mathbf{q}) + Re\Pi_\mu(\mathbf{q}, 0)$ the static limit in Eq. 1 is recovered. We show in Fig. 2 that the dynamic effects are negligible in the ZA modes.

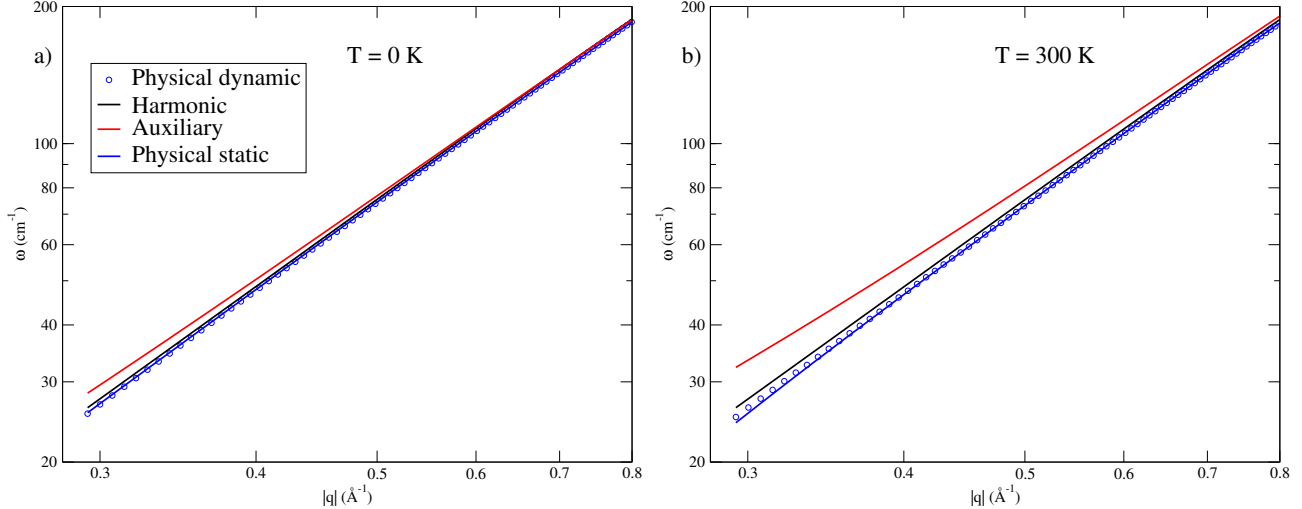


Figure 2: Harmonic, and SCHA auxiliary and physical phonons (static and dynamic) calculated at 0 K (a) and 300 K (b).

In Fig. 3 we show the root mean squared atomic displacements $\sqrt{\langle u^2 \rangle}_{\rho_{R\Phi}}$ calculated within the SCHA. Clearly, the SCHA linearization of the auxiliary ZA phonons reduces the divergences in the atomic displacements at finite temperature.

2 Empirical potential benchmark and calculation parameters

For calculating the forces needed in the SCHA minimization[1] we have used an empirical potential trained with machine learning and density functional theory (DFT) forces. The details about the machine learning training are explained in Ref. [4]. Here we have benchmarked the ability of the potential to account for the anharmonic effects. For that purpose we have applied the SCHA method by using DFT and empirical forces in a 2×2 supercell and we have checked the anharmonic effects in the optical modes at the Γ point. The machine learning potential is trained with the exchange-correlation in Ref. [5] and for the DFT calculations we have applied a PBE[6] ultrasoft pseudopotential[7] with Van der Walls corrections[8]. The results are shown in Figs. 4 and 5. As we can see in Fig. 4, the two potentials provide very similar harmonic phonons, or what is the same, very similar forces. Due to the different exchange correlation functional there is a slight offset in Fig. 5, however, the anharmonic lineshifts in both SCHA auxiliary and physical frequencies are very well captured within the empirical potential.

For the self-consistent DFT calculations we have used a plane wave cutoff of 70 Ry and a 700 Ry cutoff for the density. For the Brillouin zone integration we have used a Monkhorst pack

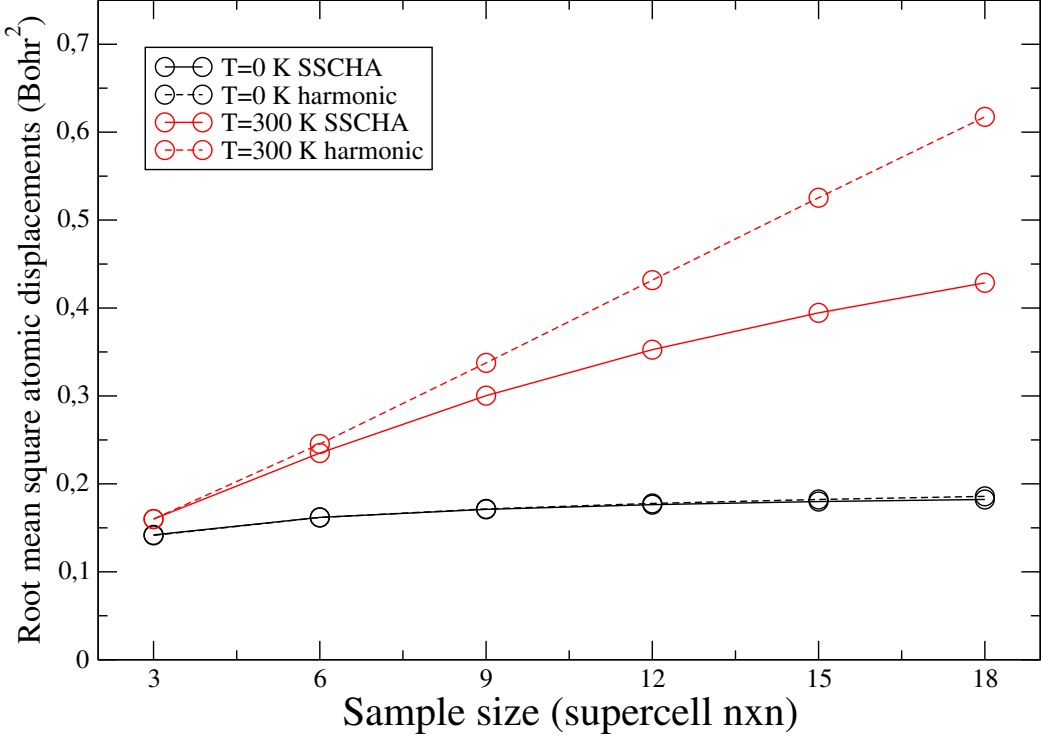


Figure 3: Harmonic and SCHA $\sqrt{\langle u^2 \rangle}$ at 0 K and 300 K.

grid[9] of 32×32 points with a Gaussian smearing of 0.02 Ry. For the linewidth calculations in the main text we have used a grid of 400×400 grid with a Gaussian smearing of 1 cm^{-1} . For the stress calculation in order to account for the thermal expansion we have used a 10×10 supercell. We have used the same supercell for the SCHA auxiliary and physical frequency calculations. For the linewidth calculations we have used 3BFC calculated in 3×3 supercells. We have tested all the calculations with denser grids and bigger supercells.

3 SCHA applied to the continuum membrane Hamiltonian

The general rotationally invariant potential for a membrane can be written as follows

$$V = \frac{1}{2} \int_{\Omega} d^2x \left(\kappa (\partial^2 h)^2 + \sum_{n \geq 2} u_{i_1 j_1} \dots u_{i_n j_n} C_{i_1 j_1 \dots i_n j_n}^{(2n)} \right), \quad (11)$$

where Ω is the area of the membrane in equilibrium, κ is the bending rigidity, h is the out-of-plane component of the displacement field and the rotationally invariant strain tensor u_{ij} is defined using the in-plane displacement field u_i

$$u_{ij} = \frac{1}{2} (\partial_i u_j + \partial_j u_i + \partial_i \mathbf{u} \cdot \partial_j \mathbf{u} + \partial_i h \partial_j h). \quad (12)$$

$C_{i_1 j_1 \dots i_n j_n}^{(2n)}$ is the generic elastic tensor of rank $2n$. In the previous expression the subscripts label the 2d coordinates x, y and the sum over indices is assumed. The second-order expansion of Eq.

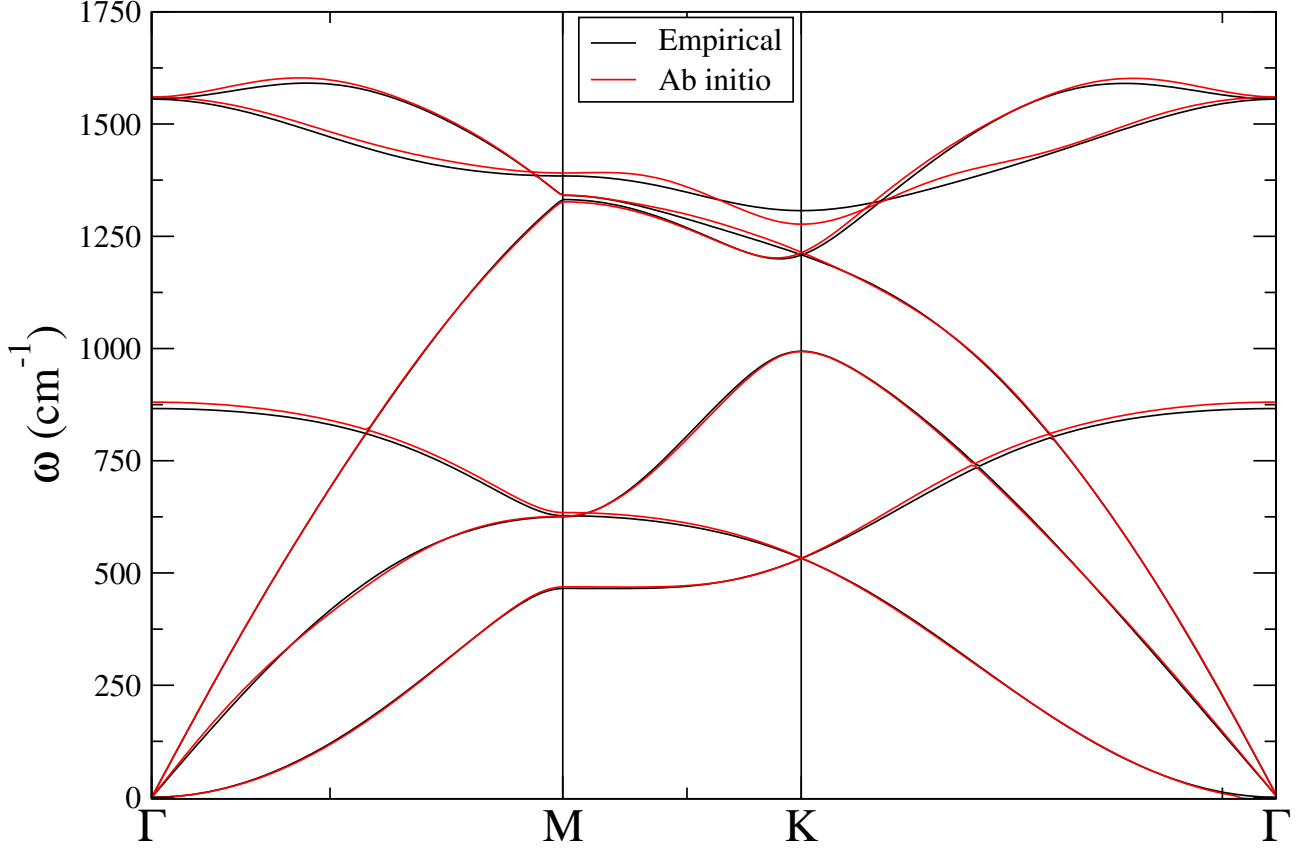


Figure 4: Harmonic phonon spectrum of graphene calculated with the empirical potential and *ab initio*. The calculations are done in a 6×6 supercell.

11 with respect to the phonon fields is given by

$$V = \frac{1}{2} \int_{\Omega} d^2x \left(\kappa(\partial^2 h)^2 + C_{ijkl}^{(4)} u_{ij} u_{il} \right), \quad (13)$$

with $C_{ijkl}^{(4)} = \lambda \delta_{ij} \delta_{kl} + \mu (\delta_{ik} \delta_{jl} + \delta_{il} \delta_{jk})$. By using equation 12 and $C_{ijkl}^{(4)} = C^{ijkl}$, equation 13 can be rewritten as

$$V = \frac{1}{2} \int_{\Omega} d^2x \left[\kappa(\partial^2 h)^2 + C^{ijkl} \partial_i u_j \partial_k u_l + C^{ijkl} \partial_i u_j \partial_k h \partial_l h + \frac{C^{ijkl}}{4} \partial_i h \partial_j h \partial_k h \partial_l h + \frac{C^{ijkl}}{2} \partial_i \mathbf{u} \cdot \partial_j \mathbf{u} \partial_k h \partial_l h + C^{ijkl} \partial_i u_j \partial_k \mathbf{u} \cdot \partial_l \mathbf{u} + \frac{C^{ijkl}}{4} \partial_i \mathbf{u} \cdot \partial_j \mathbf{u} \partial_k \mathbf{u} \cdot \partial_l \mathbf{u} \right]. \quad (14)$$

If we allow the lattice spacing a to be a variable, we can vary it by simply shifting the derivatives of the in-plane displacements according to $\partial_i u_j \rightarrow \partial_i u_j + \delta^{ij} \delta a$, where $\delta a = (a - a_0)/a_0$. Then,

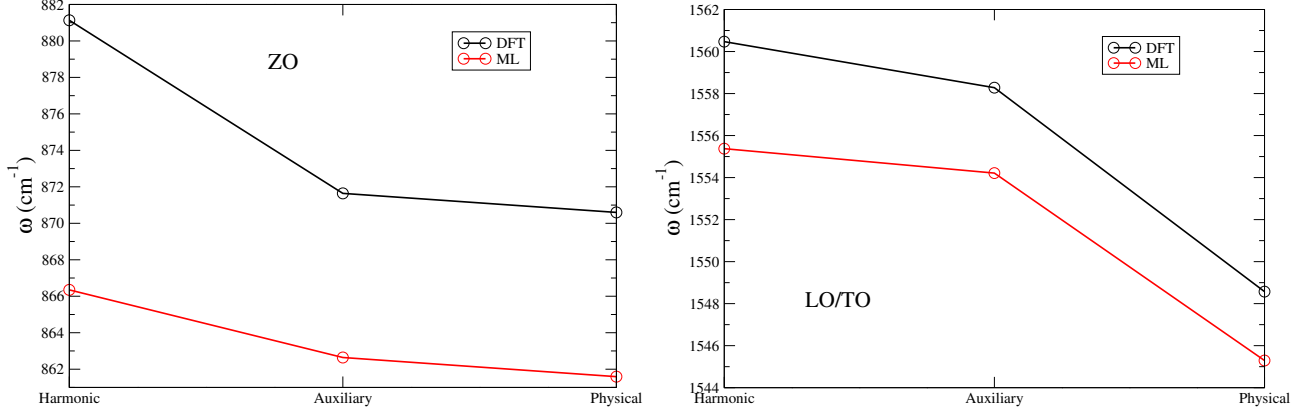


Figure 5: Harmonic, and SCHA auxiliary and physical frequencies (static) using the DFT and machine learning (ML) forces. The left panel shows the in-plane optical frequency at the Γ point and the right panel the out-of-plane one.

by taking into account periodic boundary conditions $\int_{\Omega} d^2x \partial_i u_j = 0$ we can rewrite the potential

$$\begin{aligned}
 V \rightarrow V + 2\Omega(1 + \delta a)(\lambda + \mu)\delta a^2 + (1 + \frac{\delta a}{2})\delta a(\lambda + \mu) \int_{\Omega} d^2x \partial_k h \partial_k h + \frac{\delta a}{2} \int_{\Omega} d^2x C^{ijkl} \partial_i u_j \partial_k h \partial_l h + \\
 (1 + \frac{\delta a}{2})\delta a \int_{\Omega} d^2x C^{ijkl} \partial_i u_j \partial_k u_l + (1 + \frac{\delta a}{2})\delta a(\lambda + \mu) \int_{\Omega} d^2x \partial_k \mathbf{u} \cdot \partial_k \mathbf{u} + \frac{\delta a^4 \Omega}{2}(\lambda + \mu) + \\
 \frac{\delta a}{4} \int_{\Omega} d^2x C^{ijkl} [\partial_i \mathbf{u} \cdot \partial_j \mathbf{u} \partial_k u_l + \partial_i u_j \partial_k \mathbf{u} \cdot \partial_l \mathbf{u}]. \quad (15)
 \end{aligned}$$

If we Fourier transform the potential, the SCHA free energy can be written as (we use $\hbar = k_B = 1$)

$$\begin{aligned}
\mathcal{F}(\mathcal{V}) = F_{\mathcal{V}} + 2\Omega(1 + \delta a + \frac{\delta a^2}{4})(\lambda + \mu)\delta a^2 + \frac{1}{2} \sum_{\mathbf{q}} \{g[\Omega_{SCHA}^{(h)}(\mathbf{q})]\kappa|\mathbf{q}|^4 + \{(\lambda + 2\mu)g[\Omega_{SCHA}^{(LA)}(\mathbf{q})] + \\
\mu g[\Omega_{SCHA}^{(TA)}(\mathbf{q})]\}|\mathbf{q}|^2 + \frac{\lambda + 2\mu}{4\Omega} \sum_{\mathbf{k}} g[\Omega_{SCHA}^{(h)}(\mathbf{q})]g[\Omega_{SCHA}^{(h)}(\mathbf{k})][|\mathbf{q}|^2|\mathbf{k}|^2 + 2(\mathbf{q} \cdot \mathbf{k})^2] + \\
\frac{1}{2\Omega} \sum_{\mathbf{k}} g[\Omega_{SCHA}^{(h)}(\mathbf{k})]\{g[\Omega_{SCHA}^{(LA)}(\mathbf{q})] + g[\Omega_{SCHA}^{(TA)}(\mathbf{q})]\}[\lambda|\mathbf{q}|^2|\mathbf{k}|^2 + 2\mu(\mathbf{q} \cdot \mathbf{k})^2] + \\
+ 2(1 + \frac{\delta a}{2})\delta a(\lambda + \mu)g[\Omega_{SCHA}^{(h)}(\mathbf{q})]|\mathbf{q}|^2 + 2(1 + \frac{\delta a}{2})\delta a\{(\lambda + 2\mu)g[\Omega_{SCHA}^{(LA)}(\mathbf{q})] + \mu g[\Omega_{SCHA}^{(TA)}(\mathbf{q})]\}|\mathbf{q}|^2 + \\
2(1 + \frac{\delta a}{2})\delta a(\lambda + \mu)\{g[\Omega_{SCHA}^{(LA)}(\mathbf{q})] + g[\Omega_{SCHA}^{(TA)}(\mathbf{q})]\}|\mathbf{q}|^2 - g[\Omega_{SCHA}^{(h)}(\mathbf{q})]\Phi_{SCHA}^{(h)}(\mathbf{q}) - \sum_{\alpha} g[\Omega_{SCHA}^{(\alpha)}(\mathbf{q})]\Phi_{SCHA}^{(\alpha)}(\mathbf{q}) + \\
\frac{1}{4\Omega} \sum_{\mathbf{qk}} [4g[\Omega_{SCHA}^{(LA)}(\mathbf{q})]g[\Omega_{SCHA}^{(TA)}(\mathbf{k})][\lambda(\mathbf{q} \cdot \mathbf{k})^2 + \mu|\mathbf{q}|^2|\mathbf{k}|^2 + \mu(\mathbf{q} \cdot \mathbf{k})^2](\hat{\mathbf{q}}_{\perp} \cdot \hat{\mathbf{k}}) + \\
2g[\Omega_{SCHA}^{(LA)}(\mathbf{q})]g[\Omega_{SCHA}^{(TA)}(\mathbf{k})][\lambda|\mathbf{q}|^2|\mathbf{k}|^2 + 2\mu(\mathbf{q} \cdot \mathbf{k})^2] + \\
(g[\Omega_{SCHA}^{(LA)}(\mathbf{q})]g[\Omega_{SCHA}^{(LA)}(\mathbf{k})] + g[\Omega_{SCHA}^{(TA)}(\mathbf{q})]g[\Omega_{SCHA}^{(TA)}(\mathbf{k})])[\lambda|\mathbf{q}|^2|\mathbf{k}|^2 + 2\mu(\mathbf{q} \cdot \mathbf{k})^2] + \\
2(g[\Omega_{SCHA}^{(LA)}(\mathbf{q})]g[\Omega_{SCHA}^{(LA)}(\mathbf{k})])[\lambda(\mathbf{q} \cdot \mathbf{k})^2 + \mu|\mathbf{q}|^2|\mathbf{k}|^2 + \mu(\mathbf{q} \cdot \mathbf{k})^2](\hat{\mathbf{q}} \cdot \hat{\mathbf{k}}) + \\
2(g[\Omega_{SCHA}^{(TA)}(\mathbf{q})]g[\Omega_{SCHA}^{(TA)}(\mathbf{k})])[\lambda(\mathbf{q} \cdot \mathbf{k})^2 + \mu|\mathbf{q}|^2|\mathbf{k}|^2 + \mu(\mathbf{q} \cdot \mathbf{k})^2](\hat{\mathbf{q}}_{\perp} \cdot \hat{\mathbf{k}}_{\perp})]\}, \quad (16)
\end{aligned}$$

where $g(\omega) = \coth((\omega/2T))/(2\rho\omega)$ and $\Omega_{SCHA}^{\alpha}(\mathbf{q}) = \sqrt{\Phi_{SCHA}^{(\alpha)}(\mathbf{q})/\rho}$ ($\alpha = h, LA, TA$) is the SCHA auxiliary frequency. ρ is the mass density. In Eq. 16 the in plane displacement vector $\mathbf{u}(\mathbf{q})$ is separated into longitudinal and transversal components $\mathbf{u}(\mathbf{q}) = u_{LA}(\mathbf{q})\hat{\mathbf{q}} + u_{TA}(\mathbf{q})\hat{\mathbf{q}}_{\perp}$, $\hat{\mathbf{q}}_{\perp}$ being the unitary vector perpendicular to $\hat{\mathbf{q}}$. $F_{\mathcal{V}}$ is the harmonic free energy of the harmonic trial potential \mathcal{V} . Now, by taking the derivative of the SCHA free energy with respect to the lattice constant and SCHA auxiliary frequencies, we arrive to the SCHA equations

$$\begin{aligned}
\frac{\partial \mathcal{F}(\mathcal{V})}{\partial \delta a} = 0 = 2\Omega(2\delta a + 3\delta a^2 + \delta a^3)(\lambda + \mu) + \frac{1}{2} \sum_{\mathbf{q}} g[\Omega_{SCHA}^{(h)}(\mathbf{q})]2(1 + \delta a)(\lambda + \mu)|\mathbf{q}|^2 \\
+ \frac{1}{2} \sum_{\mathbf{q}} g[\Omega_{SCHA}^{(LA)}(\mathbf{q})][2(1 + \delta a)(\lambda + 2\mu)|\mathbf{q}|^2 + 2(1 + \delta a)(\lambda + \mu)|\mathbf{q}|^2] + \\
\frac{1}{2} \sum_{\mathbf{q}} g[\Omega_{SCHA}^{(TA)}(\mathbf{q})][2(1 + \delta a)\mu|\mathbf{q}|^2 + 2(1 + \delta a/2)(\lambda + \mu)|\mathbf{q}|^2], \quad (17)
\end{aligned}$$

$$\begin{aligned}
\Phi_{SCHA}^{(h)}(\mathbf{q}) = \kappa|\mathbf{q}|^4 + 2(1 + \delta a/2)\delta a(\lambda + \mu)|\mathbf{q}|^2 + \frac{\lambda + 2\mu}{2\Omega} \sum_{\mathbf{k}} g[\Omega_{SCHA}^{(h)}(\mathbf{k})][|\mathbf{q}|^2|\mathbf{k}|^2 + 2(\mathbf{q} \cdot \mathbf{k})^2] + \\
\frac{1}{2\Omega} \sum_{\mathbf{k}} \{g[\Omega_{SCHA}^{(LA)}(\mathbf{k})] + g[\Omega_{SCHA}^{(TA)}(\mathbf{k})]\}[\lambda|\mathbf{q}|^2|\mathbf{k}|^2 + 2\mu(\mathbf{q} \cdot \mathbf{k})^2], \quad (18)
\end{aligned}$$

$$\begin{aligned}
\Phi_{SCHA}^{(LA)}(\mathbf{q}) = & (\lambda + 2\mu)|\mathbf{q}|^2 + 2(1 + \delta a/2)\delta a(\lambda + 2\mu)|\mathbf{q}|^2 + 2(1 + \delta a/2)\delta a(\lambda + \mu)|\mathbf{q}|^2 \\
+ \frac{1}{2\Omega} \sum_{\mathbf{k}} g[\Omega_{SCHA}^{(h)}(\mathbf{k})][\lambda|\mathbf{q}|^2|\mathbf{k}|^2 + 2\mu(\mathbf{q} \cdot \mathbf{k})^2] + \frac{1}{4\Omega} \sum_{\mathbf{k}} \{4g[\Omega_{SCHA}^{(TA)}(\mathbf{k})][\lambda(\mathbf{q} \cdot \mathbf{k})^2 + \mu|\mathbf{q}|^2|\mathbf{k}|^2 + \mu(\mathbf{q} \cdot \mathbf{k})^2](\hat{\mathbf{q}}_{\perp} \cdot \hat{\mathbf{k}}) + \\
2g[\Omega_{SCHA}^{(TA)}(\mathbf{k})][\lambda|\mathbf{q}|^2|\mathbf{k}|^2 + 2\mu(\mathbf{q} \cdot \mathbf{k})^2] + \\
2g[\Omega_{SCHA}^{(LA)}(\mathbf{k})][\lambda|\mathbf{q}|^2|\mathbf{k}|^2 + 2\mu(\mathbf{q} \cdot \mathbf{k})^2] + \\
4g[\Omega_{SCHA}^{(LA)}(\mathbf{k})][\lambda(\mathbf{q} \cdot \mathbf{k})^2 + \mu|\mathbf{q}|^2|\mathbf{k}|^2 + \mu(\mathbf{q} \cdot \mathbf{k})^2](\hat{\mathbf{q}} \cdot \hat{\mathbf{k}})\} \quad (19)
\end{aligned}$$

and,

$$\begin{aligned}
\Phi_{SCHA}^{(TA)}(\mathbf{q}) = & \mu|\mathbf{q}|^2 + 2(1 + \delta a/2)\delta a\mu|\mathbf{q}|^2 + 2(1 + \delta a/2)\delta a(\lambda + \mu)|\mathbf{q}|^2 \\
+ \frac{1}{2\Omega} \sum_{\mathbf{k}} g[\Omega_{SCHA}^{(h)}(\mathbf{k})][\lambda|\mathbf{q}|^2|\mathbf{k}|^2 + 2\mu(\mathbf{q} \cdot \mathbf{k})^2] + \frac{1}{4\Omega} \sum_{\mathbf{k}} \{4g[\Omega_{SCHA}^{(TA)}(\mathbf{k})][\lambda(\mathbf{q} \cdot \mathbf{k})^2 + \mu|\mathbf{q}|^2|\mathbf{k}|^2 + \mu(\mathbf{q} \cdot \mathbf{k})^2](\hat{\mathbf{q}}_{\perp} \cdot \hat{\mathbf{k}}_{\perp})] + \\
4g[\Omega_{SCHA}^{(LA)}(\mathbf{k})][\lambda(\mathbf{q} \cdot \mathbf{k})^2 + \mu|\mathbf{q}|^2|\mathbf{k}|^2 + \mu(\mathbf{q} \cdot \mathbf{k})^2](\hat{\mathbf{q}}_{\perp} \cdot \hat{\mathbf{k}}) + \\
2g[\Omega_{SCHA}^{(TA)}(\mathbf{k})][\lambda|\mathbf{q}|^2|\mathbf{k}|^2 + 2\mu(\mathbf{q} \cdot \mathbf{k})^2]\}. \quad (20)
\end{aligned}$$

We have solved this equations in a circular grid with 60×60 \mathbf{q} points with a radius of 1 \AA^{-1} by applying the Newton-Raphson method[10]. We have checked the convergency of the results with denser grids. The parameters which have been calculated by using the atomistic empirical potential are the following: $\lambda = 4.3 \text{ eV\AA}^{-2}$, $\mu = 9.3 \text{ eV\AA}^{-2}$, $\kappa = 1.5 \text{ eV}$ and, $\rho/\hbar^2 = 1097 \text{ eV\AA}^{-4}$. This model accounts for the negative thermal expansion of graphene as it can be seen

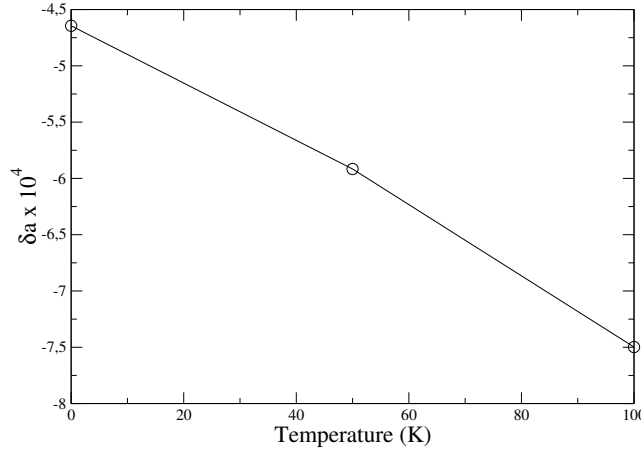


Figure 6: δa as a function of temperature in the membrane model.

in Fig. 6.

Regarding the second derivative of the free energy, the physical phonons in the static approach, the most general formula for the correction to the SCHA auxiliary phonon frequencies

is

$$D_{\alpha\beta}^{corr}(-\mathbf{q}, \mathbf{q}) = \sum_{\gamma\delta\epsilon\zeta} \sum_{\mathbf{p}\mathbf{k}} {}^{(3)}D_{\alpha\gamma\delta}(-\mathbf{q}, \mathbf{p}, \mathbf{q} - \mathbf{p}) [1 - {}^{(4)}D_{\gamma\delta\epsilon\zeta}(-\mathbf{p}, \mathbf{p} - \mathbf{q}, \mathbf{k}, \mathbf{q} - \mathbf{k})]^{-1} {}^{(3)}D_{\epsilon\zeta\beta}(-\mathbf{k}, \mathbf{k} - \mathbf{q}, \mathbf{q}), \quad (21)$$

where the subindexes run on the normal coordinates $\alpha, \beta, \gamma, \delta, \epsilon, \zeta = h, u_{LA}, u_{TA}$ and the dynamical matrices in normal coordinates are defined as

$${}^{(3)}D_{\alpha\beta\gamma}(\mathbf{q}, \mathbf{k}, \mathbf{p}) = \frac{1}{\rho^{3/2}} \left\langle \frac{\partial^3 V}{\partial\alpha(\mathbf{q})\partial\beta(\mathbf{k})\partial\gamma(\mathbf{p})} \right\rangle_{\rho_V} \sqrt{G_{\beta\gamma}(\mathbf{k}, \mathbf{p})}, \quad (22)$$

$${}^{(4)}D_{\alpha\beta\gamma\epsilon}(\mathbf{q}, \mathbf{q}', \mathbf{k}, \mathbf{k}') = \frac{1}{\rho^2} \left\langle \frac{\partial^4 V}{\partial\alpha(\mathbf{q})\partial\beta(\mathbf{q}')\partial\gamma(\mathbf{k})\partial\epsilon(\mathbf{k}')} \right\rangle_{\rho_V} \sqrt{G_{\alpha\beta}(\mathbf{q}, \mathbf{k})G_{\gamma\epsilon}(\mathbf{q}', \mathbf{k}')}. \quad (23)$$

The matrix $G_{\alpha\beta}(\mathbf{q}, \mathbf{k})$ is defined as

$$G_{\alpha\beta}(\mathbf{q}, \mathbf{k}) = \frac{F(0, \Omega_{SCHA}^\alpha(\mathbf{q}), \Omega_{SCHA}^\beta(\mathbf{k}))}{\Omega_{SCHA}^\alpha(\mathbf{q})\Omega_{SCHA}^\beta(\mathbf{k})}, \quad (24)$$

$F(0, \Omega_{SCHA}^\alpha(\mathbf{q}), \Omega_{SCHA}^\beta(\mathbf{k}))$ being the function defined in Eq. 4. We are interested in the corrections to the out-of-plane modes, therefore, we are interested in the terms of the type

$$D_{hh}^{corr}(-\mathbf{q}, \mathbf{q}) = \sum_{\gamma\delta\epsilon\zeta} \sum_{\mathbf{p}\mathbf{k}} {}^{(3)}D_{h\gamma\delta}(-\mathbf{q}, \mathbf{p}, \mathbf{q} - \mathbf{p}) [1 - {}^{(4)}D_{\gamma\delta\epsilon\zeta}(-\mathbf{p}, \mathbf{p} - \mathbf{q}, \mathbf{k}, \mathbf{q} - \mathbf{k})]^{-1} {}^{(3)}D_{\epsilon\zeta h}(-\mathbf{k}, \mathbf{k} - \mathbf{q}, \mathbf{q}), \quad (25)$$

By looking at Eq. 15 we can see that only the terms of the type $\int_\Omega d^2x C^{ijkl} \partial_i u_j \partial_k h \partial_l h$ will contribute to the statistical average in Eq. 22. Therefore, Eq. 21 can be rewritten as

$$D_{hh}^{corr}(-\mathbf{q}, \mathbf{q}) = 4 \sum_{\alpha\beta} \sum_{\mathbf{p}\mathbf{k}} {}^{(3)}D_{h\alpha h\beta}(-\mathbf{q}, \mathbf{p}, \mathbf{q} - \mathbf{p}) [1 - {}^{(4)}D_{h\alpha h\beta}(-\mathbf{p}, \mathbf{p} - \mathbf{q}, \mathbf{k}, \mathbf{q} - \mathbf{k})]^{-1} {}^{(3)}D_{h\beta h}(-\mathbf{k}, \mathbf{k} - \mathbf{q}, \mathbf{q}), \quad (26)$$

where now the subindexes only run in $\alpha, \beta = u_{LA}, u_{TA}$. Now, we can calculate the statistical averages

$$\left\langle \frac{\partial^3 V}{\partial h(\mathbf{k}_1)\partial h(\mathbf{k}_2)\partial u_{LA}(\mathbf{k}_3)} \right\rangle_{\rho_V} = \frac{1 + \delta a}{\sqrt{\Omega}} \delta_{\mathbf{k}_1 + \mathbf{k}_2 + \mathbf{k}_3, 0} \left[\lambda |\mathbf{k}_3| \mathbf{k}_1 \cdot \mathbf{k}_2 + 2\mu \frac{(\mathbf{k}_3 \cdot \mathbf{k}_1)(\mathbf{k}_3 \cdot \mathbf{k}_2)}{|\mathbf{k}_3|} \right], \quad (27)$$

$$\left\langle \frac{\partial^3 V}{\partial h(\mathbf{k}_1)\partial h(\mathbf{k}_2)\partial u_{TA}(\mathbf{k}_3)} \right\rangle_{\rho_V} = \frac{\mu(1 + \delta a)}{\sqrt{\Omega}} \delta_{\mathbf{k}_1 + \mathbf{k}_2 + \mathbf{k}_3, 0} \left[\frac{(\mathbf{k}_3 \cdot \mathbf{k}_1)(\mathbf{k}_{3\perp} \cdot \mathbf{k}_2) + (\mathbf{k}_3 \cdot \mathbf{k}_2)(\mathbf{k}_{3\perp} \cdot \mathbf{k}_1)}{|\mathbf{k}_3|} \right], \quad (28)$$

$$\left\langle \frac{\partial^4 V}{\partial h(\mathbf{k}_1)\partial h(\mathbf{k}_2)\partial u_{LA}(\mathbf{k}_3)\partial u_{LA}(\mathbf{k}_4)} \right\rangle_{\rho_V} = \frac{1}{\Omega} \delta_{\mathbf{k}_1 + \mathbf{k}_2 + \mathbf{k}_3 + \mathbf{k}_4, 0} \frac{\mathbf{k}_3 \cdot \mathbf{k}_4}{|\mathbf{k}_3||\mathbf{k}_4|} [\lambda(\mathbf{k}_3 \cdot \mathbf{k}_4)(\mathbf{k}_1 \cdot \mathbf{k}_2) + \mu(\mathbf{k}_3 \cdot \mathbf{k}_1)(\mathbf{k}_4 \cdot \mathbf{k}_2) + \mu(\mathbf{k}_3 \cdot \mathbf{k}_2)(\mathbf{k}_4 \cdot \mathbf{k}_1)], \quad (29)$$

$$\left\langle \frac{\partial^4 V}{\partial h(\mathbf{k}_1) \partial h(\mathbf{k}_2) \partial u_{TA}(\mathbf{k}_3) \partial u_{TA}(\mathbf{k}_4)} \right\rangle_{\rho_V} = \frac{1}{\Omega} \delta_{\mathbf{k}_1 + \mathbf{k}_2 + \mathbf{k}_3 + \mathbf{k}_4, 0} \frac{\mathbf{k}_{3\perp} \cdot \mathbf{k}_{4\perp}}{|\mathbf{k}_3| |\mathbf{k}_4|} [\lambda(\mathbf{k}_3 \cdot \mathbf{k}_4)(\mathbf{k}_1 \cdot \mathbf{k}_2) + \mu(\mathbf{k}_3 \cdot \mathbf{k}_1)(\mathbf{k}_4 \cdot \mathbf{k}_2) + \mu(\mathbf{k}_3 \cdot \mathbf{k}_2)(\mathbf{k}_4 \cdot \mathbf{k}_1)], \quad (30)$$

and

$$\left\langle \frac{\partial^4 V}{\partial h(\mathbf{k}_1) \partial h(\mathbf{k}_2) \partial u_{LA}(\mathbf{k}_3) \partial u_{TA}(\mathbf{k}_4)} \right\rangle_{\rho_V} = \frac{1}{\Omega} \delta_{\mathbf{k}_1 + \mathbf{k}_2 + \mathbf{k}_3 + \mathbf{k}_4, 0} \frac{\mathbf{k}_3 \cdot \mathbf{k}_{4\perp}}{|\mathbf{k}_3| |\mathbf{k}_4|} [\lambda(\mathbf{k}_3 \cdot \mathbf{k}_4)(\mathbf{k}_1 \cdot \mathbf{k}_2) + \mu(\mathbf{k}_3 \cdot \mathbf{k}_1)(\mathbf{k}_4 \cdot \mathbf{k}_2) + \mu(\mathbf{k}_3 \cdot \mathbf{k}_2)(\mathbf{k}_4 \cdot \mathbf{k}_1)]. \quad (31)$$

The equations cannot be further simplified but we have all the ingredients to calculate them numerically. We have checked numerically that, as in the atomistic case, the contribution of $\overset{(4)}{\mathbf{D}}$ is completely negligible.

By making use of the dynamical ansatz explained in section 1, the linewidths of LA and TA modes can be calculated within the SCHA. In the main text we have calculated the linewidths as shown in section 1, where the fourth-order tensor is neglected in Eq. 6. Now we will prove that neglecting the fourth-order tensor and assuming the Lorentzian approximation are good approximations. For that purpose we Taylor expand Eq. 6

$$\Pi(z) = \mathbf{M}^{-\frac{1}{2}} \overset{(3)}{\Phi} \Lambda(z) [\mathbf{1} - \overset{(4)}{\Phi} \Lambda(z)]^{-1} \overset{(3)}{\Phi} \mathbf{M}^{-\frac{1}{2}} \simeq \mathbf{M}^{-\frac{1}{2}} \overset{(3)}{\Phi} \Lambda(z) \overset{(3)}{\Phi} \mathbf{M}^{-\frac{1}{2}} + \mathbf{M}^{-\frac{1}{2}} \overset{(3)}{\Phi} \Lambda(z) \overset{(4)}{\Phi} \Lambda(z) \overset{(3)}{\Phi} \mathbf{M}^{-\frac{1}{2}} + \dots, \quad (32)$$

and we calculate the contribution of the term containing the fourth-order tensor to the linewidth. We also calculate the spectral function with and without including the frequency dependence of the self energy. We show the results in Fig. 7. The figure clearly shows that the contribution

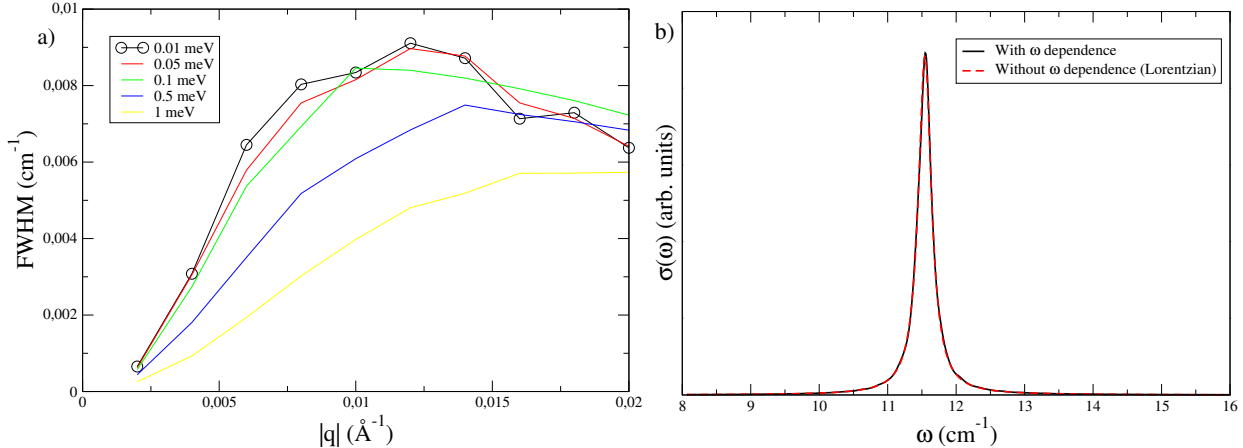


Figure 7: (a) Linewidth (full width at half maximum, FWHM) contribution of the term containing the fourth-order tensor of the LA mode calculated in the membrane model at 100 K using the harmonic and SCHA auxiliar phonons. The value of the smearing is in the legend. (b) Spectral function of the LA mode with momentum 0.01 \AA^{-1} with and without considering the frequency dependence of the self energy.

of the fourth-order tensor is at least one order of magnitude smaller than the main term and,

what it is more important, it also decays as momentum decreases. The figure also shows that the Lorentzian approximation is justified for the acoustic modes in graphene.

By neglecting the fourth-order terms containing in-plane displacement fields in Eq. 11, the SCHA can be applied analytically in this model. The SCHA equations simplify to

$$\delta a = -\frac{1}{4\Omega} \sum_{\mathbf{q}} |\mathbf{q}|^2 g[\Omega_{SCHA}^{(h)}(\mathbf{q})], \quad (33)$$

$$\Phi_{SCHA}^{(h)}(\mathbf{q}) = \kappa |\mathbf{q}|^4 + 2\delta a(\lambda + \mu) |\mathbf{q}|^2 + \frac{\lambda + 2\mu}{2\Omega} \sum_{\mathbf{k}} g[\Omega_{SCHA}^{(LA)}(\mathbf{k})] [|\mathbf{q}|^2 |\mathbf{k}|^2 + 2(\mathbf{q} \cdot \mathbf{k})^2]. \quad (34)$$

By inserting Eq. 33 in Eq. 34 and considering the infinite volume limit ($\Omega \rightarrow \infty$), we obtain

$$\Phi_{SCHA}^{(h)}(\mathbf{q}) = \kappa |\mathbf{q}|^4 + \gamma |\mathbf{q}|^2, \quad (35)$$

where γ is given by the solution of

$$\gamma = \gamma \frac{\lambda + 3\mu}{16\pi\kappa\sqrt{\rho\kappa}} \int_0^{\Lambda\sqrt{\kappa/\gamma}} ds \frac{s^2 \coth[\gamma s \sqrt{1+s^2}/(2T\sqrt{\rho\kappa})]}{\sqrt{1+s^2}}. \quad (36)$$

Λ is an ultraviolet cutoff that avoids divergencies. Eqs. 35 and 36 show that the dispersion of the SCHA auxiliary ZA modes is linear. By calculating the correction for getting the physical phonons in the static approach in Eq. 26 (in this case the fourth-order tensor is 0) the result is

$$\Phi_F^{(h)}(\mathbf{q}) = \kappa |\mathbf{q}|^4 + (\gamma - \sigma) |\mathbf{q}|^2 + O(|\mathbf{q}|^4), \quad (37)$$

where at $T = 0$ K

$$\sigma = \frac{\rho\sqrt{\gamma}}{8\pi\kappa^{3/2}} \sum_{\alpha=LA,TA} v_{\alpha} f(\Lambda\sqrt{\kappa/\gamma}, v_{\alpha}\sqrt{\rho/\gamma}), \quad (38)$$

with

$$f(x, y) = \int_0^x ds \frac{s^2}{\sqrt{1+s^2} [\sqrt{1+s^2} + y]}. \quad (39)$$

By setting the ultraviolet cutoff to the value of the Debye momentum, $\Lambda = \sqrt{\frac{8\pi}{3^{1/2}a_0}} = 1.55\text{\AA}$, we obtain $1 - \sigma/\gamma = 20\%$. This means that the linear component of the physical frequencies turns out to be a factor of 40% smaller than the one of the SCHA auxiliary frequency. The non zero linear term in the physical frequencies appears because neglecting the fourth-order terms including in-plane displacements breaks the rotational invariance of the potential.

References

[1] Ion Errea, Matteo Calandra, and Francesco Mauri. Anharmonic free energies and phonon dispersions from the stochastic self-consistent harmonic approximation: Application to platinum and palladium hydrides. *Physical Review B*, 89(6):064302, 2014.

- [2] Raffaello Bianco, Ion Errea, Lorenzo Paulatto, Matteo Calandra, and Francesco Mauri. Second-order structural phase transitions, free energy curvature, and temperature-dependent anharmonic phonons in the self-consistent harmonic approximation: Theory and stochastic implementation. *Physical Review B*, 96(1):014111, 2017.
- [3] Lorenzo Monacelli, Ion Errea, Matteo Calandra, and Francesco Mauri. Pressure and stress tensor of complex anharmonic crystals within the stochastic self-consistent harmonic approximation. *Physical Review B*, 98(2):024106, 2018.
- [4] Patrick Rowe, Gábor Csányi, Dario Alfè, and Angelos Michaelides. Development of a machine learning potential for graphene. *Physical Review B*, 97(5):054303, 2018.
- [5] Max Dion, Henrik Rydberg, Elsebeth Schröder, David C Langreth, and Bengt I Lundqvist. Van der waals density functional for general geometries. *Physical review letters*, 92(24):246401, 2004.
- [6] John P Perdew, Kieron Burke, and Matthias Ernzerhof. Generalized gradient approximation made simple. *Physical review letters*, 77(18):3865, 1996.
- [7] David Vanderbilt. Soft self-consistent pseudopotentials in a generalized eigenvalue formalism. *Physical review B*, 41(11):7892, 1990.
- [8] Vincenzo Barone, Maurizio Casarin, Daniel Forrer, Michele Pavone, Mauro Sambi, and Andrea Vittadini. Role and effective treatment of dispersive forces in materials: Polyethylene and graphite crystals as test cases. *Journal of computational chemistry*, 30(6):934–939, 2009.
- [9] Hendrik J Monkhorst and James D Pack. Special points for brillouin-zone integrations. *Physical review B*, 13(12):5188, 1976.
- [10] Tjalling J Ypma. Historical development of the newton–raphson method. *SIAM review*, 37(4):531–551, 1995.